Biophysical Journal, Volume 98

Supporting Material

A multiscale red blood cell model with accurate mechanics, rheology and dynamics

Dmitry A. Fedosov, Bruce Caswell, and George Karniadakis

Supporting Material

January 20, 2010

RBC recovery test

To study dynamics of RBC recovery after stretching with force f, we introduce the time-dependent elongational index $e(t)$ analogously to that in (1) as follows

$$e(t) = \frac{(\lambda - \lambda_\infty)(\lambda_0 + \lambda_\infty)}{(\lambda + \lambda_\infty)(\lambda_0 - \lambda_\infty)} = \exp\left[-\left(\frac{t}{t_c}\right)^\delta\right], \tag{1}$$

where $\lambda = D_A/D_T$, λ_0 and λ_∞ correspond to the ratios at times $t = 0.0$ and $t = \infty$, t_c is the characteristic time, and δ is the exponent (*Note that in (1) $\delta = 1$, and thus equation (1) is a generalization of the equation (11) in (1)*). Similar to the creep test, the time scale exponent is set to $\alpha = 0.75$. Figure 1 (left) shows RBC recovery after deformation by the force 7 pN with $\eta_m = 0.022\ Pa \cdot s$. In the case of $\delta = 1$ we observe a

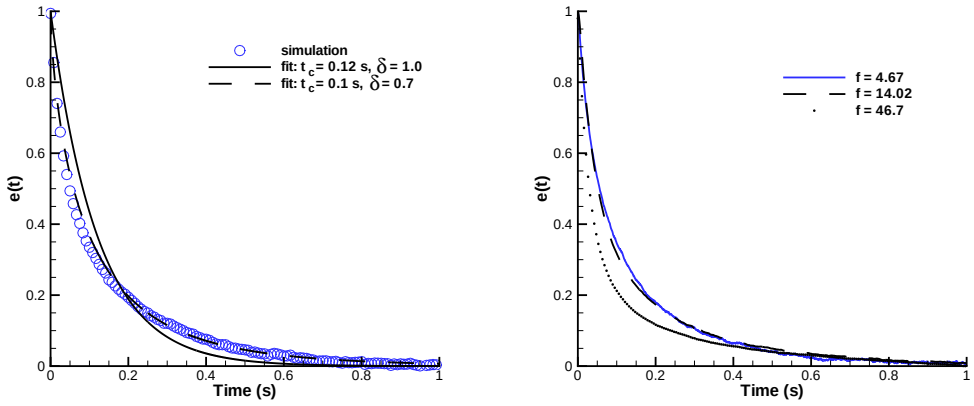

Figure 1: RBC recovery after deformation by the force of $f = 7\ pN$ for different fits (left) and after different stretching forces (right).

rather poor fit to the RBC recovery, while the fit with $\delta = 0.7$ yields excellent agreement with the recovery dynamics. Figure 1 (right) demonstrates sensitivity of the recovery dynamics to the total stretching force (or initial stretch). The response appears to be not sensitive to small initial stretches, however the RBC recovery response is different for the case of a high initial stretch, where non-linear effects may be present. In addition, we note that RBC recovery showed a long tail decay and it is important to have a long enough sample to correctly measure λ_∞, which may greatly affect fitting parameters. Thus, the experiments on RBC recovery has to be followed for at least several seconds, in contrast to the RBC recovery (1) observed over approximately $0.5\ s$.

Dissipative Particle Dynamics

Dissipative Particle Dynamics (DPD) (2, 3) is a mesoscopic particle method, where each particle represents a *molecular cluster* rather than an individual atom, and can be thought of as a soft lump of fluid. The DPD system consists of N point particles of mass m_i, position $\mathbf{r}_i$ and velocity $\mathbf{v}_i$. DPD particles interact through three forces: conservative ($\mathbf{F}_{ij}^C$), dissipative ($\mathbf{F}_{ij}^D$), and random ($\mathbf{F}_{ij}^R$) forces given by

$$\begin{aligned} \mathbf{F}_{ij}^C &= F_{ij}^C(r_{ij})\hat{\mathbf{r}}_{ij}, \\ \mathbf{F}_{ij}^D &= -\gamma\omega^D(r_{ij})(\mathbf{v}_{ij}\cdot\hat{\mathbf{r}}_{ij})\hat{\mathbf{r}}_{ij}, \\ \mathbf{F}_{ij}^R &= \sigma\omega^R(r_{ij})\frac{\xi_{ij}}{\sqrt{dt}}\hat{\mathbf{r}}_{ij}, \end{aligned} \tag{2}$$

where $\hat{\mathbf{r}}_{ij} = \mathbf{r}_{ij}/r_{ij}$, and $\mathbf{v}_{ij} = \mathbf{v}_i - \mathbf{v}_j$. The coefficients γ and σ define the strength of dissipative and random forces, respectively. In addition, ω^D and ω^R are weight functions, and ξ_{ij} is a normally distributed random variable with zero mean, unit variance, and $\xi_{ij} = \xi_{ji}$. All forces are truncated beyond the cutoff radius r_c, which defines the length scale in the DPD system. The conservative force is given by

$$F_{ij}^C(r_{ij}) = \begin{cases} a_{ij}(1 - r_{ij}/r_c) & for \quad r_{ij} \le r_c, \\ 0 & for \quad r_{ij} > r_c, \end{cases} \tag{3}$$

where a_{ij} is the conservative force coefficient between particles i and j.

The random and dissipative forces form a thermostat and must satisfy the fluctuation-dissipation theorem in order for the DPD system to maintain equilibrium temperature T (4). This leads to:

$$\omega^D(r_{ij}) = \left[\omega^R(r_{ij})\right]^2, \qquad \sigma^2 = 2\gamma k_B T, \tag{4}$$

where k_B is the Boltzmann constant. The choice for the weight functions is as follows

$$\omega^R(r_{ij}) = \begin{cases} (1 - r_{ij}/r_c)^k & for \quad r_{ij} \le r_c, \\ 0 & for \quad r_{ij} > r_c, \end{cases} \tag{5}$$

where $k = 1$ for the original DPD method. However, other choices (e.g., $k = 0.25$) for these envelopes have been used (5, 6) in order to increase the viscosity of the DPD fluid.

The time evolution of velocities and positions of particles is determined by the Newton's second law of motion

$$d\mathbf{r}_i = \mathbf{v}_i dt, \tag{6}$$

$$d\mathbf{v}_i = \frac{1}{m_i}\sum_{j\neq i}\left(\mathbf{F}_{ij}^C + \mathbf{F}_{ij}^D + \mathbf{F}_{ij}^R\right)dt. \tag{7}$$

The above equations of motion were integrated using the modified velocity-Verlet algorithm (2).

RBC model framework

The average equilibrium shape of a RBC is biconcave as measured experimentally (7), and is represented by

$$z = \pm D_0\sqrt{1 - \frac{4(x^2+y^2)}{D_0^2}}\left[a_0 + a_1\frac{x^2+y^2}{D_0^2} + a_2\frac{(x^2+y^2)^2}{D_0^4}\right], \tag{8}$$

where $D_0 = 7.82\ \mu m$ is the average diameter, $a_0 = 0.0518$, $a_1 = 2.0026$, and $a_2 = -4.491$. The surface area and volume of this RBC are equal to $135\ \mu m^2$ and $94\ \mu m^3$, respectively.

In the simulations, the membrane network structure is generated by triangulating the unstressed equilibrium shape described by (8). The cell shape is first imported into a commercial grid generation software to produce an initial triangulation based on the advancing-front method. Subsequently, free-energy relaxation is performed by flipping the diagonals of quadrilateral elements formed by two adjacent triangles, while the vertices are constrained to move on the prescribed surface. The relaxation procedure includes only elastic in-plane and bending energy components.

The membrane model is constructed as a set of vertex points $\{\mathbf{x}_i\}$, $i \in 1...N_v$. The potential energy of the system $V(\{\mathbf{x}_i\})$ is described in the paper. Particle forces are derived from the above energies as follows

$$\mathbf{f}_i = -\partial V(\{\mathbf{x}_i\})/\partial \mathbf{x}_i, \qquad i \in 1...N_v. \tag{9}$$

Exact force expressions can be found in (8).

Mechanical properties

Theoretical analysis of a hexagonal network is presented to derive linear macroscopic properties of the network. We extend the linear analysis of a two-dimensional sheet of springs built with equilateral triangles (9). Figure 2 presents an element of the hexagonal network where vertex **v** is placed at the origin. From the

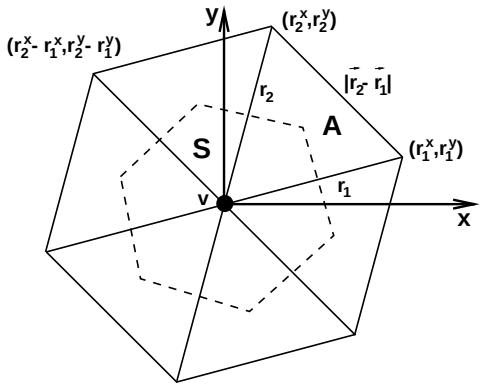

Figure 2: An element of the hexagonal triangulation.

virial theorem, the Cauchy stress at the vertex **v** surrounded by the area element S is given by

$$\begin{aligned}\tau_{\alpha\beta} = -\frac{1}{S}\left[\frac{f(r_1)}{r_1} r_1^\alpha r_1^\beta + \frac{f(r_2)}{r_2} r_2^\alpha r_2^\beta + \frac{f(|\vec{r_2} - \vec{r_1}|)}{|\vec{r_2} - \vec{r_1}|}(r_2^\alpha - r_1^\alpha)(r_2^\beta - r_1^\beta)\right] - \\ - \left(\frac{k_a(A_0^{tot} - N_t A)}{A_0^{tot}} + \frac{k_d(A_0 - A)}{A_0}\right)\delta_{\alpha\beta},\end{aligned} \tag{10}$$

where $f(\cdot)$ is the spring force, α, β are x or y, N_t is the total number of triangles, $A_0^{tot} = N_t A_0$, and $S = 2A_0$. Substitution of A_0^{tot} for the global area contribution to the stress allows us to combine it with the local area term as $-(k_a + k_d)(A_0 - A)/A_0 \delta_{\alpha\beta}$. The linear shear modulus is derived from a network deformation by applying the engineering shear strain γ,

$$\vec{r_1'} = \vec{r_1} J = (r_1^x + r_1^y \gamma/2;\ r_1^x \gamma/2 + r_1^y), \quad J = \begin{pmatrix} 1 & \gamma/2 \\ \gamma/2 & 1 \end{pmatrix}. \tag{11}$$

The shear deformation is area-preserving, and therefore only spring forces contribute to the membrane shear modulus. Expansion of τ_{xy} in Taylor series provides the linear shear modulus of the network as follows

$$\tau'_{xy} = \tau_{xy} + \left.\frac{\partial \tau'_{xy}}{\partial \gamma}\right|_{\gamma=0} \gamma + O(\gamma^2), \quad \mu_0 = \left.\frac{\partial \tau'_{xy}}{\partial \gamma}\right|_{\gamma=0}. \tag{12}$$

As an example of differentiation we obtain

$$\left.\frac{\partial \left(\frac{f(r'_1)}{r'_1} r_1^{x'} r_1^{y'}\right)}{\partial \gamma}\right|_{\gamma=0} = \left.\left(\frac{\partial \frac{f(r_1)}{r_1}}{\partial r_1} \frac{(r_1^x r_1^y)^2}{r_1} + \frac{f(r_1) r_1}{2}\right)\right|_{r_1=l_0}. \tag{13}$$

Using a geometrical argument it can be shown that $(r_1^x r_1^y)^2 + (r_2^x r_2^y)^2 + (r_2^x - r_1^x)^2 (r_2^y - r_1^y)^2 = 2A_0^2$. Equations (12) and (13) allow us to derive the linear shear modulus of the network given in the paper.

The linear-elastic area-compression modulus K is calculated from a small area expansion with the resulting in-plane pressure given by

$$P = -\frac{1}{2}(\tau_{xx} + \tau_{yy}) = \frac{3lf(l)}{4A} + \frac{(k_a + k_d)(A_0 - A)}{A_0}. \tag{14}$$

With the compression modulus K defined as

$$K = -\left.\frac{\partial P}{\partial \log(A)}\right|_{A=A_0} = -\left.\frac{1}{2}\frac{\partial P}{\partial \log(l)}\right|_{l=l_0} = -\left.\frac{1}{2}\frac{\partial P}{\partial \log(x)}\right|_{x=x_0}, \tag{15}$$

we use equations (14) and (15) to derive the linear area-compression modulus shown in the paper.

The area-compression modulus is much larger than the shear modulus for a nearly area-incompressible material. The Young's modulus Y of the two-dimensional sheet can be found as follows

$$Y = \frac{4K\mu_0}{K + \mu_0}, \qquad Y \to 4\mu_0, \;\; if \;\; K \to \infty, \tag{16}$$

with the Poisson's ratio ν given by

$$\nu = \frac{K - \mu_0}{K + \mu_0}, \qquad \nu \to 1, \;\; if \;\; K \to \infty. \tag{17}$$

In order to satisfy the area-incompressibility assumption we have set $k_a + k_d \gg \mu_0$, while in practice, the values of $\mu_0 = 100$ and $k_a + k_d = 5000$ are used, that provide nearly area-incompressible membrane with Young's modulus about 2% smaller than its asymptotic value of $4\mu_0$. The analytical expressions were verified through a number of numerical tests using a regular two-dimensional sheet of springs. Note the two-dimensional sheet is *isotropic* for shear and stretching linear-deformations, while *anisotropy* is found at large deformations.

Membrane bending rigidity

In this section we discuss the correspondence of our bending model to the macroscopic model of Helfrich (10) given by

$$E = \frac{k_c}{2} \int_A (C_1 + C_2 - 2C_0)^2 dA + k_g \int_A C_1 C_2 dA, \tag{18}$$

where C_1 and C_2 are the local principal curvatures, C_0 is the spontaneous curvature, and k_c and k_g are the bending rigidities.

We base the derivation on the spherical shell. Figure 3 shows two equilateral triangles with sides a, whose vertices rest on the surface of a sphere of radius R. The angle between their normals $\mathbf{n}_1$ and $\mathbf{n}_2$ is

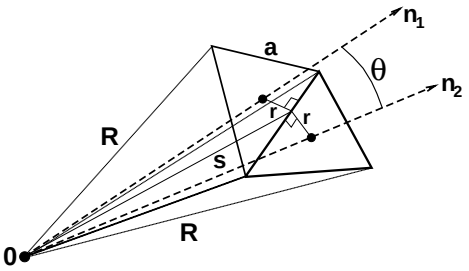

Figure 3: Two equilateral triangles placed on the surface of a sphere of radius R.

equal to θ. For the spherical shell we can derive from equation (18) $E = 8\pi k_c(1 - C_0/C_1)^2 + 4\pi k_g = 8\pi k_c(1 - R/R_0)^2 + 4\pi k_g$, where $C_1 = C_2 = 1/R$ and $C_0 = 1/R_0$. For the triangulated sphere we have $E_t = N_s k_b[1 - cos(\theta - \theta_0)]$ in the defined notations. We expand $cos(\theta - \theta_0)$ in Taylor series around $(\theta - \theta_0)$ to obtain $E_t = N_s k_b(\theta - \theta_0)^2/2 + O((\theta - \theta_0)^4)$. From figure 3 we find that $2r \approx \theta R$ or $\theta = \frac{a}{\sqrt{3}R}$, and analogously $\theta_0 = \frac{a}{\sqrt{3}R_0}$. Furthermore, $A_{sphere} = 4\pi R^2 \approx N_t A_0 = \frac{\sqrt{3}N_t a^2}{4} = \frac{N_s a^2}{2\sqrt{3}}$, and thus $a^2/R^2 = 8\pi\sqrt{3}/N_s$. Finally, we obtain $E_t = N_s k_b(\frac{a}{\sqrt{3}R} - \frac{a}{\sqrt{3}R_0})^2/2 = \frac{N_s k_b a^2}{6R^2}(1 - R/R_0)^2 = \frac{8\pi k_b}{2\sqrt{3}}(1 - R/R_0)^2$. Equating the macroscopic bending energy E for $k_g = -4k_c/3$, $C_0 = 0$ (11) and E_t gives us the relation $k_b = 2k_c/\sqrt{3}$ in agreement with the continuum limit in (11). The spontaneous angle θ_0 is set according to the total number of vertices N_v on the sphere. It can be shown that $\cos(\theta) = 1 - \frac{1}{6(R^2/a^2 - 1/4)} = (\sqrt{3}N_s - 10\pi)/(\sqrt{3}N_s - 6\pi)$, while $N_s = 2N_v - 4$. The corresponding bending stiffness k_b and the spontaneous angle θ_0 are then given by

$$k_b = \frac{2}{\sqrt{3}}k_c, \qquad \theta_0 = cos^{-1}\left(\frac{\sqrt{3}(N_v - 2) - 5\pi}{\sqrt{3}(N_v - 2) - 3\pi}\right). \tag{19}$$

RBC-solvent boundary conditions

The RBC membrane encloses a volume of fluid and is itself suspended in a solvent. In particle methods, such as DPD, fluids are represented as a collection of interacting particles. Thus, in order to impose appropriate boundary conditions (BCs) between the membrane and the external/internal fluids two matters need to be addressed:

i) enforcement of membrane impenetrability to prevent mixing of the inner and the outer fluids,

ii) no-slip BCs imposed through pairwise point interactions between the fluid particles and the membrane vertices.

Membrane impenetrability is enforced by imposing bounce-back reflection of fluid particles at the moving membrane triangular plaquettes. The bounce-back reflection enhances the no-slip boundary conditions at the membrane surface as compared to specular reflection; however, it does not guarantee no-slip. Additional dissipation enhancement between the fluid and the membrane is required to achieve no-slip at the membrane boundary. For this purpose, the DPD dissipative force between fluid particles and membrane vertices needs to be properly set based on the idealized case of linear shear flow over a flat plate. In continuum, the total shear force exerted by the fluid on the area A is equal to $A\eta\dot{\gamma}$, where η is the fluid's viscosity and $\dot{\gamma}$ is the local wall shear-rate. In DPD, we distribute a number of particles on the wall to mimic the membrane vertices. The force on a single wall particle exerted by the sheared fluid can be found as follows

$$F_v = \int_{V_h} n g(r) F^D dV, \tag{20}$$

where F^D is the DPD dissipative force (12) between fluid particles and membrane vertices, n is the fluid number density, $g(r)$ is the radial distribution function of fluid particles with respect to the wall particles, and V_h is the half sphere volume of fluid above the wall. Here, the total shear force on the area A is equal to $N_A F_v$, where N_A is the number of wall particles enclosed by A. The equality of $N_A F_v = A\eta\dot{\gamma}$ results in an expression of the dissipative force coefficient in terms of the fluid density and viscosity, and the wall density N_A/A, while under the assumption of linear shear flow the shear rate $\dot{\gamma}$ cancels out. This formulation results in satisfaction of the no-slip BCs for the linear shear flow over a flat plate. It also serves as an excellent approximation for no-slip at the membrane surface in spite of the assumptions made. Note that in the absence of conservative interactions between fluid and wall particles $g(r) = 1$.

System sizes and computer times

The developed parallel code is based on LAMMPS Molecular Dynamics Simulator (13) distributed by Sandia National Laboratories as an open source code under the terms of the GPL license. The DPD code was built up on top of LAMMPS. Table 1 shows examples of system sizes and computer times. The system

simulation	system size (particles)	processors	timesteps	computational time (s)
TTC	3587	4	500000	3623
Thermal fluctuations	3500	4	1000000	7112
Couette flow	24500	16	1050000	12254
Poiseuille flow	6587	8	500000	3412

Table 1: System sizes and computer times.

size corresponds to the total number of particles N including RBC vertices and those representing the internal/external fluids. The computational time scales linearly with N.

References

1. Hochmuth, R. M., P. R. Worthy, and E. A. Evans, 1979. Red cell extensional recovery and the determination of membrane viscosity. *Biophysical Journal* 26:101–114.

2. Groot, R. D., and P. B. Warren, 1997. Dissipative particle dynamics: Bridging the gap between atomistic and mesoscopic simulation. *Journal of Chemical Physics* 107:4423–4435.

3. Hoogerbrugge, P. J., and J. M. V. A. Koelman, 1992. Simulating microscopic hydrodynamic phenomena with dissipative particle dynamics. *Europhysics Letters* 19:155–160.

4. Espanol, P., and P. Warren, 1995. Statistical mechanics of dissipative particle dynamics. *Europhysics Letters* 30:191–196.

5. Fedosov, D. A., I. V. Pivkin, and G. E. Karniadakis, 2008. Velocity Limit in DPD Simulations of Wall-Bounded Flows. *Journal of Computational Physics* 227:2540–2559.

6. Fan, X., N. Phan-Thien, S. Chen, X. Wu, and T. Y. Ng, 2006. Simulating flow of DNA suspension using dissipative particle dynamics. *Physics of Fluids* 18:063102.

7. Evans, E. A., and R. Skalak, 1980. Mechanics and thermodynamics of biomembranes. CRC Press, Inc., Boca Raton, Florida.

8. Fedosov, D. A., 2010. Multiscale modeling of blood flow and soft matter. *PhD thesis* Brown University, USA.

9. Dao, M., J. Li, and S. Suresh, 2006. Molecularly based analysis of deformation of spectrin network and human erythrocyte. *Materials Science and Engineering C* 26:1232–1244.

10. Helfrich, W., 1973. Elastic properties of lipid bilayers: theory and possible experiments. *Z. Naturforschung C* 28:693–703.

11. Lidmar, J., L. Mirny, and D. R. Nelson, 2003. Virus shapes and buckling transitions in spherical shells. *Physical Review E* 68:051910.

12. Espanol, P., 1998. Fluid particle model. *Physical Review E* 57:2930–2948.

13. LAMMPS Molecular Dynamics Simulator. Sandia National Laboratories, http://lammps.sandia.gov.